

# ATMOSPHERIC PRESSURE AND MOLECULAR CLOUD FORMATION IN EARLY-TYPE GALAXIES

IU. V. BABYK<sup>1,2,3,4\*</sup>, B. R. MCNAMARA<sup>2,3,5</sup>, P. E. J. NULSEN<sup>6,7</sup>, H. R. RUSSELL<sup>8</sup>, A. C. EDGE<sup>9</sup>, AND LEO BLITZ<sup>10</sup>

<sup>1</sup> Department of Physics and Astronomy, University of California at Irvine, 4129 Frederick Reines Hall, Irvine, CA 92697, USA

<sup>2</sup> Department of Physics and Astronomy, University of Waterloo, 200 University Avenue West, Waterloo, ON, N2L 3G1, Canada

<sup>3</sup> Waterloo Center for Astrophysics, University of Waterloo, 200 University Avenue West, Waterloo, ON, N2L 3G1, Canada

<sup>4</sup> Main Astronomical Observatory of the National Academy of Sciences of Ukraine, 27 Zabolotnoho str., 03143, Kyiv, Ukraine

<sup>5</sup> Perimeter Institute for Theoretical Physics, Waterloo, ON, N2L 2Y5, Canada

<sup>6</sup> Harvard-Smithsonian Center for Astrophysics, 60 Garden Street, Cambridge, MA 02138, USA

<sup>7</sup> ICRAR, University of Western Australia, 35 Stirling Hwy, Crawley, WA 6009, Australia

<sup>8</sup> Institute of Astronomy, Madingley Road, Cambridge CB3 0HA, UK

<sup>9</sup> Department of Physics, University of Durham, South Road, Durham DH1 3LE, United Kingdom

<sup>10</sup> Department of Astronomy, University of California, Berkeley, CA 94720, USA

*Draft version November 2, 2021*

## ABSTRACT

A strong correlation between atmospheric pressure and molecular gas mass is found in central cluster galaxies and early-type galaxies. This trend and a similar trend with atmospheric gas density would naturally arise if the molecular clouds condensed from hot atmospheres. Limits on the ratio of molecular to atomic hydrogen in these systems exceed unity. The data are consistent with ambient pressure being a significant factor in the rapid conversion of atomic hydrogen into molecules as found in normal spiral galaxies.

**Keywords:** galaxies: clusters: intracluster medium galaxies: X-rays

## 1. INTRODUCTION

Central cluster and elliptical galaxies contain gas over a broad range of temperature. The most abundant form resides in a hot atmosphere with temperatures of  $10^7$  K– $10^8$  K maintained close to hydrostatic equilibrium. Cooler ionized gas above  $10^4$  K (Bregman et al. 2006; Crawford et al. 1999; McDonald et al. 2010, 2011), atomic (O’Dea et al. 1998; Welch et al. 2010; Oosterloo et al. 2010; Putman et al. 2012; Westmeier 2018) and molecular gas at colder temperatures are present in smaller amounts. (Edge 2001; Edge et al. 2002; Salomé & Combes 2003, 2004; Salomé et al. 2006; Donahue et al. 2011; Pulido et al. 2018; Russell et al. 2019; Olivares et al. 2019).

This gas and its phases may originate from several sources including, stellar mass loss, accretion from other galaxies, accretion from the intergalactic medium, and primordial gas remaining from the early moments of galaxy formation (Bregman 2007; Dekel et al. 2009). Some of this gas may end up in the hot phase as it is heated by shocks to the virial temperature of the halo. Recent analyses indicate that a significant fraction of the molecular gas in early type and central cluster galaxies may be produced by atmospheric cooling from the hot phase gas (Werner et al. 2019; Babyk et al. 2019; Pulido et al. 2018). Absent continual energy input, the hot atmosphere will radiate away its thermal energy and condense onto the host galaxy, fueling both star formation and feedback from nuclear black holes (Fabian 1994, 2012; McNamara & Nulsen 2007, 2012). This development is significant. Observational and theoretical considerations indicate that the growth of massive galaxies is both suppressed and regulated by feedback from supermassive black holes and stellar winds (Croton et al. 2006; Sijacki et al. 2007; Bower et al. 2006a; Behroozi et al. 2013). Self-regulated growth via black hole feedback requires a steady

supply of fuel to self-regulate. Self regulation would be difficult to maintain if cold fuel arrived stochastically, as expected for mergers and inflow from the intergalactic medium. Therefore understanding the origins of all gas phases in galaxies is central to understanding how galaxies themselves have evolved.

Why cold gas in central cluster galaxies is predominantly molecular hydrogen rather than atomic hydrogen is poorly understood. Early searches for HI at the centers of clusters revealed only upper limits (Haynes & Roberts 1979; McNamara et al. 1990; O’Dea et al. 1994). The limits were sufficient to exclude the notion that atmospheres were cooling at their radiative rates and settling into the atomic gas. These small surveys detected atomic hydrogen in absorption in several objects indicating the presence of some atomic hydrogen. Targeting clusters identified by the Rosat All Sky Survey, Edge et al. (2002) and Salomé & Combes (2003) discovered molecular clouds in great abundance at the centers of clusters with the highest radiative cooling rates. The amounts, despite exceeding  $10^{10} M_{\odot}$ , are too low to account for atmospheric cooling at unimpeded rates. Nevertheless, the relatively high molecular gas masses indicated that hot atmospheres were indeed likely to be cooling significantly with the cooling gas being converted efficiently from atoms to molecules.

Molecules form primarily on dust grains, even those with relatively high kinetic temperatures (Le Bourlot et al. 2012). Unshielded dust would sputter away rapidly in the harsh cluster environment (Draine & Salpeter 1979). Nevertheless, dust is abundant in the star formation and molecular gas complexes located at the centers of clusters (Vantyghem et al. 2018; Donahue et al. 2011; Russell et al. 2019; Olivares et al. 2019). Dust is also abundant in giant elliptical galaxies (Sadler & Gerhard 1985; Goudfrooij et al. 1994; van Dokkum & Franx 1995). It is usually associated with cold atomic and molecular gas (Combes et al. 2007). Thirty to forty percent of early-type galaxies contain detectable levels of molecular gas (Combes

\* babikyura@gmail.com

et al. 2007; Salomé et al. 2011; Young et al. 2011). Infrared and radio observations indicate that a minority of systems with relatively large amounts of molecular gas form stars at rates of  $\sim 0.1 \text{ M}_{\odot} \text{ yr}^{-1}$  or so (Combes et al. 2007; Shapiro et al. 2010; Ford & Bregman 2013). Despite the harsh atmospheric environment, conditions are evidently ripe for dust and molecular gas formation.

The efficiency of conversion from HI to  $\text{H}_2$  depends critically on the strength of the radiation field and the pressure of the surrounding interstellar medium (Elmegreen 1993). Apparently, even a slight increase in pressure can convert an entire HI cloud into molecular gas. Conversely, increased levels of ultraviolet radiation can quickly dissociate molecular hydrogen into a mostly neutral phase. Large regions of the interstellar medium may transform quickly into molecules when experiencing increased pressure in spiral arms (Elmegreen 1993). Molecules may then return to atoms in the higher photon density regions of star formation. Studying spiral galaxies with a variety of morphologies, Blitz & Rosolowsky (2006) and Leroy et al. (2008) found a strong correlation between the surface density ratio of  $\text{H}_2/\text{HI}$  such that the ratio increases well above unity with increasing midplane pressure. This trend has been studied previously only in spiral galaxies. Here we examine the relationship between hydrostatic pressure and molecular gas abundance in a relatively large sample of central cluster galaxies and normal ellipticals.

## 2. DATA

### 2.1. X-rays

Data taken from Hogan et al. (2017); Pulido et al. (2018); Babyk et al. (2019, 2018) were used to extract hydrostatic pressure profiles for the objects studied here. These works include 110 clusters and 58 groups and galaxies sufficiently nearby and with enough exposure time to resolve the thermodynamic properties of the inner regions ( $< 10 \text{ kpc}$ ) of their atmospheres. Descriptions of the data reduction procedures, spectral fitting, and the calculation of the pressure profiles can be found in Hogan et al. (2017); Pulido et al. (2018); Babyk et al. (2019, 2018). Here we summarize briefly.

Data reduction, including reprocessing and bad pixel extraction, were performed using the CIAO v4.2 software package. To create cleaned, level-2 event files, the CHANDRA\_REPRO tool was applied. The ACIS\_PROCESS\_EVENTS tool was used to correct the time-dependent gain, while the LC\_CLEAN tool provided by M. Markevitch was used to detect and remove the background flares. We used the WAVDETECT tool to identify and remove point sources. Each observation has been processed with the corresponding blank-sky background file. Multiple observations were reprojected to match the observation with the longest exposure time. The X-ray spectra were extracted using circular annuli and then deprojected using the DSDEPROJ routine (Russell et al. 2008). The ancillary response and response matrix files were extracted using MKWARF and MKACISRMF tools. The chip gaps and the area lost to point sources were corrected with exposure maps.

The projected and deprojected spectra have been fitted using XSPEC v12.8 software (Arnaud 1996). The spectral modeling has been performed using an absorbed thermal model. The projected and deprojected temperature and spectral normalization were used to measure atmospheric density, which in turn were used to calculate hydrostatic pressure.

### 2.2. Atomic and molecular Gas

**Table 1**

$\text{H}_2$  and HI estimates of our sample. References: [1] - Serra et al. (2019), [2] - Chung et al. (2009), [3] - Annis & Jewitt (1993), [4] - McNamara et al. (1990).

| Name    | $\text{H}_2$<br>$\times 10^7 M_{\odot}$ | HI<br>$\times 10^7 M_{\odot}$ | Ref. |
|---------|---|-------------------------------|------|
| NGC1316 | $60.8 \pm 4.9$                          | $4.4 \pm 0.4$                 | [1]  |
| NGC4374 | $0.57 \pm 0.2$                          | $< 1.8$                       | [2]  |
| NGC4261 | $< 4.9$                                 | $< 49.0$                      | [2]  |
| NGC4382 | $< 2.5$                                 | $< 0.9$                       | [2]  |
| NGC4472 | $0.06 \pm 0.01$                         | $< 0.7$                       | [2]  |
| NGC4552 | $< 1.9$                                 | $< 0.7$                       | [2]  |
| NGC4649 | $< 2.8$                                 | $< 1.5$                       | [2]  |
|         | $\times 10^{10} M_{\odot}$              | $\times 10^9 M_{\odot}$       |      |
| A1795   | $0.39 \pm 0.04$                         | $< 5.2$                       | [4]  |
| A1991   | $0.88 \pm 0.05$                         | $< 3.6$                       | [4]  |
| A2052   | $0.30 \pm 0.03$                         | $< 3.5$                       | [4]  |
| A2204   | $3.3 \pm 0.12$                          | $< 1.1$                       | [4]  |
| A2597   | $1.3 \pm 0.4$                           | $< 4.3$                       | [4]  |
| A262    | $0.39 \pm 0.02$                         | $< 1.2$                       | [4]  |
| A496    | $0.72 \pm 0.03$                         | $< 4.7$                       | [4]  |
| Hydra-A | $1.1 \pm 0.03$                          | $< 0.84$                      | [4]  |
| A2029   | $1.3 \pm 0.05$                          | $< 11.0$                      | [4]  |
| AWM7    | $0.28 \pm 0.02$                         | $< 2.2$                       | [4]  |

Molecular gas masses were taken from Pulido et al. (2018) and Babyk et al. (2019). Molecular gas mass measurements were available for 76 targets, including 21 for the low-mass systems (mostly ellipticals). The CO data were obtained from a variety of instruments. Pulido’s sample included IRAM data while Babyk’s sample included both IRAM and ALMA data. Note that only 9 low-mass objects are detected in CO, while the remaining 11 are upper limits. In the case of central cluster galaxies (BCGs) we include 17 upper limits.

The situation for HI mass measurements is worse. Only one HI emission detection, NGC1316, (Serra et al. 2019), is available. The remaining 16 HI measurements are upper limits McNamara et al. (1990); Chung et al. (2009). We are able to explore the  $\text{H}_2/\text{HI}$  – P relation for only 17 targets listed in Table 1. While this number is low, we have assembled enough measurements to explore this relationship in a statistically meaningful fashion.

## 3. COLD GAS MASS VS. HYDROSTATIC PRESSURE

The relationship between molecular gas mass and hydrostatic pressure is shown in Fig. 3. Hydrostatic pressure is measured at a characteristic radius of 10 kpc. Measuring the pressure at 10 kpc ensures the temperature and density measurements are well resolved in all targets over the observed redshift range. We examined data at radii of 1 and 5 kpc to determine how the trends depend on radius. The inner bin was adopted when resolution prevented us from making a measurement at 1 kpc. All trends remain qualitatively similar and do not depend on choice of radius, as indicated in Table 2. The temperature and density correlations shown in Fig. 2, studied earlier in Pulido et al. (2018) and Babyk et al. (2019), are used to examine the scatter in pressure. The correlations

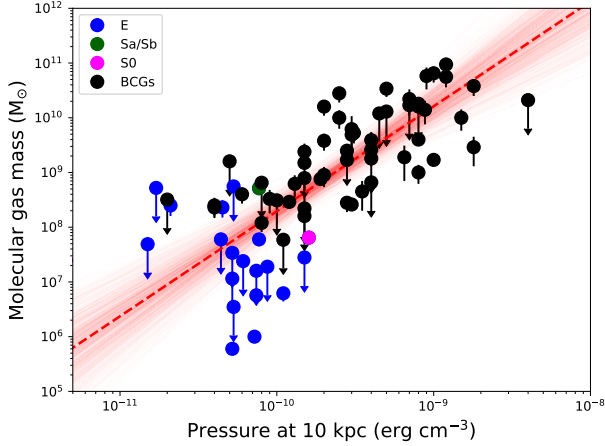


**Figure 1.** The cold molecular gas mass plotted against the pressure at 10 kpc. The red dashed and solid lines represent best-fit slope and its uncertainties respectively.

between pressure and density are tighter than with temperature. The density trend is tightest. The increased scatter in the pressure plot is due to the scatter in temperature, which in turn is related to halo mass. Applying the likelihood-based approach of Kelly (2007), the  $M_{mol}-P$  relation follows a power-law with a slope of  $1.9 \pm 0.3$ . The uncertainties of the best-fit parameters were calculated by running 15000 iterations of MCMC. We use several statistical approaches to test this relation for normality. Fit parameters including slopes and normalizations, uncertainties,  $p$ -values for null-hypotheses, and intrinsic scatter are given in Table 2. The plot is shown in Fig. 3. A similar slope of 1.9 is found for density vs molecular gas mass (Babyk et al. 2019).

Both the pressure and density trends with molecular gas mass may be understood in the context of cooling from the hot atmosphere. For an ideal hot system, the cooling rate of the atmosphere scales as  $\dot{M} \propto \rho_{Atm}^2 T^{1/2} \propto P^2 T^{-3/2}$ , where  $\rho_{Atm}$  is the atmospheric electron density and  $p$  is the hydrostatic pressure. In cooler systems, like most of those discussed here, cooling scales quadratically with density and pressure but with temperature scaling as  $\dot{M} \propto \rho_{Atm}^2 T^{-1/2} \propto P^2 T^{-5/2}$ . Therefore, both density and pressure should scale almost quadratically with the total cold gas mass. This scaling ignores metallicity variations and assumes unimpeded cooling which are unlikely to hold over the lives of these systems. Nevertheless the trend in is roughly consistent with this scaling with gas density and pressure being the dominant factors. Molecular clouds presumably accumulated from net cooling over the past  $\sim$  Gyr or so. Cooling is almost certainly the origin of the molecular gas in cluster central galaxies. Its origins in lower-mass atmospheres of early type galaxies, which have more scatter about their scaling relations (Babyk et al. 2019; Lakhchaura et al. 2018; Werner et al. 2019), are less certain. Nevertheless, the correlation with pressure for the early-type galaxies is consistent with the cluster centrals and is somewhat tighter than the  $M_{mol}-M_X$  relation Babyk et al. (2019).

#### 4. $H_2$ /HI MASS RATIO DEPENDENCE ON HYDROSTATIC PRESSURE

The link between cold gas mass and atmospheric cooling applies to the total cold gas mass including the atomic and molecular phases. The prevalence of molecular hydrogen indicates that most of the cold gas is molecular. This may be

related to high pressures at the bases of hot atmospheres, as it is in spirals.

The relationship between the neutral atomic gas mass and hydrostatic pressure at 10 kpc is shown in Fig. 3. The left panel shows HI mass vs pressure in cgs units, while the right panel shows the mass ratio of  $H_2$ /HI for systems with both CO and HI observations taken from the literature. With only one HI detection we are unable to explore this ratio in detail. However, the lower limits may be meaningfully compared to spiral galaxies with measurements of both gas phases. The range of neutral gas mass limits for both clusters and early-type galaxies is quite large, spanning  $10^7$ - $10^{10} M_\odot$ . This range is comparable to the observed range of molecular gas masses.

No significant trend between pressure and HI mass limit is found. The right panel of Fig. 3, shows the  $H_2$ /HI mass ratio vs pressure. Here pressure is expressed in units of Kelvin  $\text{cm}^{-3}$  to compare to spiral galaxy midplane pressures from the literature. The gray region and solid line represent the sample and best-fit result of Blitz & Rosolowsky (2006) and Leroy et al. (2008), respectively, for spiral galaxies. The ratio  $H_2$ /HI should be expressed in surface density units rather than mass. However, the upper limits and unresolved detection do not permit the surface densities of HI and  $H_2$  to be measured. We assume then that the HI and  $H_2$  are nearly cospatial, which may not always be true.

Fig. 3 indicates that the only detection lies within the pressure region found for spirals by Blitz & Rosolowsky (2006). The lower limits for  $H_2$ /HI mass are also consistent with the dependence on midplane pressure found for spirals by Blitz and Leroy. Our measurements were fit with a single power-law, similarly to the  $M_{mol}-P$  relation, using survival analysis. Survival analysis accounts for uncertainties in both detections and upper limits in order to estimate the form and likelihood of a relationship (Feigelson & Nelson 1985; Isobe et al. 1986; Schmitt 1985).

The likelihood is given as

$$L = \prod_{i=1}^n \text{Prob}[t_i, \delta_i] = \prod_{i=1}^n [f(t_i)^{\delta_i}] [1 - S(t_i)]^{1-\delta_i}, \quad (1)$$

where,  $t_i = \min(x_i, c_i)$ ,  $x_i$  are the detected values,  $c_i$  are the upper limits,  $\delta_i$  is 0 for upper limits and 1 for detections. The  $f_i$  and  $S_i$  are the likelihoods for detections and upper limits, respectively. In the case of a Gaussian error distribution, the likelihood for detections is given by

$$f(x) = \frac{1}{\sqrt{2\pi}\sigma} \exp \left[ -\frac{1}{2} \left( \frac{x-\mu}{\sigma} \right)^2 \right], \quad (2)$$

where,  $x$  and  $\sigma$  are the detected values of molecular gas mass and their errors, while  $\mu$  is the model. The likelihood for upper limits  $S(x)$  is

$$S(x) = 1 - \frac{1}{2} \left[ 1 + \text{erf} \left( \frac{x-\mu}{\sqrt{2}\sigma} \right) \right], \quad (3)$$

where erf is the error function,  $\text{erf}(x) = \frac{2}{\sqrt{\pi}} \int_0^x e^{-t^2} dt$ . In the case of Eq. 3 we use  $x = (\text{upper limit})_i$  and  $\sigma = (\text{upper limit})_{i=1,2,3,..}$ , where 1, 2, 3, .. indicate upper limits at the  $1\sigma, 2\sigma, 3\sigma..$  confidence intervals, respectively.

The optimum slope found by applying this method is  $0.83 \pm 0.19$  for 3 sigma confidence. This value is consistent with Blitz & Rosolowsky (2004, 2006) who found the disc

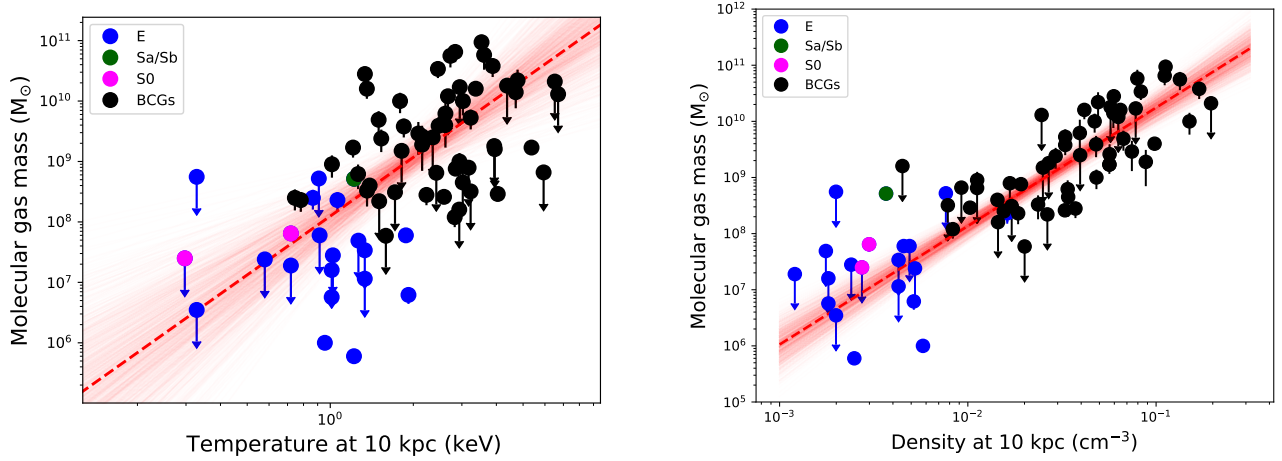


**Figure 2.** The cold molecular gas mass plotted against temperature (left) and electron density (right) at 10 kpc.

**Table 2**  
 $M_{mol} - P$  and  $H_2/HI - P$  relations of the form  $\log(y) = a + b \log(x)$  for features defined at 1, 5, and 10 kpc.

| Relation        | $a$              | $b$             | $p$ -Pearson | $p$ -Spearman | $p$ -AD | $p$ -SW | Intr. scatter |
|-----------------|------------------|-----------------|--------------|---------------|---------|---------|---------------|
| at 10 kpc       |                  |                 |              |               |         |         |               |
| $M_{mol} - P$   | $13.08 \pm 0.04$ | $1.9 \pm 0.3$   | $>> 0.0001$  | $>> 0.0001$   | 0.97    | 1.61    | $0.9 \pm 0.2$ |
| $H_2/HI - P$    | $11.66 \pm 0.23$ | $0.83 \pm 0.19$ | $>> 0.0001$  | $>> 0.0001$   | 0.92    | 1.27    | $1.2 \pm 0.4$ |
| $M_{mol} - kT$  | $8.09 \pm 0.27$  | $3.24 \pm 0.78$ | $>> 0.0001$  | $>> 0.0001$   | 0.95    | 1.33    | $1.3 \pm 0.3$ |
| $M_{mol} - n_e$ | $12.89 \pm 0.25$ | $2.35 \pm 0.15$ | $>> 0.0001$  | $>> 0.0001$   | 0.98    | 1.22    | $0.4 \pm 0.1$ |
| at 1 kpc        |                  |                 |              |               |         |         |               |
| $M_{mol} - P$   | $24.12 \pm 1.95$ | $1.7 \pm 0.2$   | $>> 0.0001$  | $>> 0.0001$   | 0.99    | 1.75    | $0.7 \pm 0.2$ |
| $H_2/HI - P$    | $12.62 \pm 0.33$ | $0.85 \pm 0.22$ | $>> 0.0001$  | $>> 0.0001$   | 0.96    | 1.18    | $1.5 \pm 0.5$ |
| $M_{mol} - kT$  | $8.19 \pm 0.20$  | $3.22 \pm 0.50$ | $>> 0.0001$  | $>> 0.0001$   | 0.97    | 1.42    | $0.8 \pm 0.2$ |
| $M_{mol} - n_e$ | $11.04 \pm 0.38$ | $2.15 \pm 0.33$ | $>> 0.0001$  | $>> 0.0001$   | 0.97    | 1.74    | $0.7 \pm 0.2$ |
| at 5 kpc        |                  |                 |              |               |         |         |               |
| $M_{mol} - P$   | $26.51 \pm 2.50$ | $1.9 \pm 0.3$   | $>> 0.0001$  | $>> 0.0001$   | 0.96    | 1.51    | $0.8 \pm 0.2$ |
| $H_2/HI - P$    | $12.23 \pm 0.33$ | $0.88 \pm 0.29$ | $>> 0.0001$  | $>> 0.0001$   | 0.95    | 1.43    | $1.1 \pm 0.3$ |
| $M_{mol} - kT$  | $8.08 \pm 0.23$  | $3.35 \pm 0.58$ | $>> 0.0001$  | $>> 0.0001$   | 0.98    | 1.53    | $0.9 \pm 0.3$ |
| $M_{mol} - n_e$ | $11.11 \pm 0.27$ | $2.26 \pm 0.20$ | $>> 0.0001$  | $>> 0.0001$   | 0.99    | 1.38    | $0.5 \pm 0.1$ |

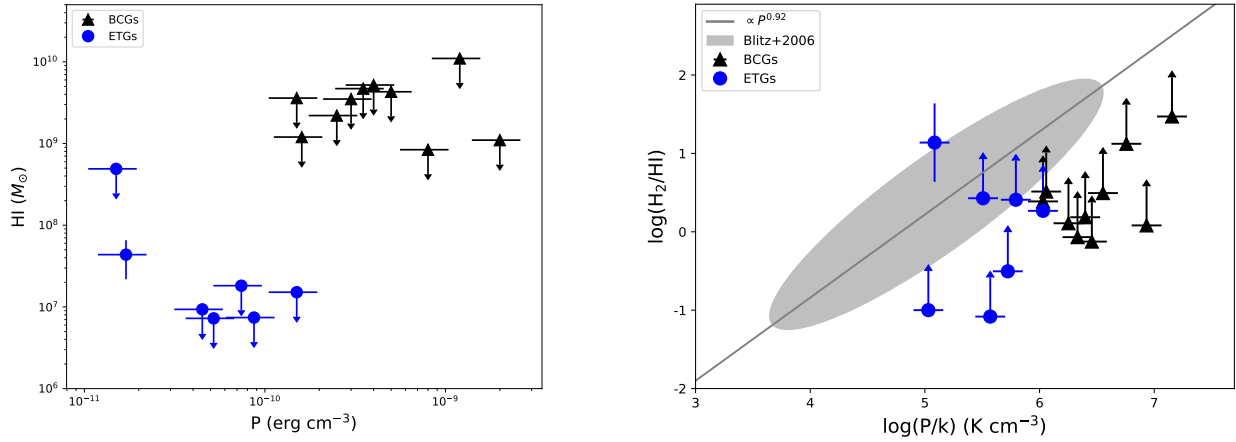


**Figure 3.** Left: The atomic gas mass plotted against hydrostatic pressure at 10 kpc. Right: The ratio of cold molecular gas mass to neutral atomic gas mass plotted against hydrostatic pressure.



midplane pressure scales with molecular and atomic gas ratio as

$$R_{H_2} = \left( \frac{\sum_{H_2}}{\sum_{HI}} \right) = \left( \frac{P_m}{P_0} \right)^\alpha. \quad (4)$$

Here,  $\sum_{H_2}$  and  $\sum_{HI}$  are the  $H_2$  and HI surface densities, respectively.  $P_m$  is the midplane pressure of the disk (Blitz & Rosolowsky 2006; Krumholz et al. 2012).  $P_0$  and  $\alpha$  are the free power-law parameters. Blitz & Rosolowsky (2006) found that  $H_2/HI \propto P^{0.92}$ .  $P_0 = 2.3 \times 10^4$  (cm<sup>-3</sup> k) is the pressure above which the ratio of  $H_2/HI$  mass surface densities exceeds unity. All cluster and early-type galaxy systems examined here lie well above this pressure.

Current instrumentation struggles to detect HI in these systems which hampers our ability to achieve a more detailed picture. Nevertheless, the HI upper limits emphasize the key point that these systems are depleted in HI relative to  $H_2$ . The application of survival statistics to a data set of this size indicates consistency with data from Blitz & Rosolowsky (2006).

#### 4.1. Discussion

Central galaxies have yielded high fidelity measurements of star formation, gas in all phases, and remarkably precise measurements of AGN feedback power. They are iconic systems that have provided the deepest insights into the complex cycles of feedback and galaxy-black hole co-evolution that likely occur in all massive galaxies. The systems studied here are experiencing radio/mechanical feedback that prevents the atmospheres from cooling catastrophically. Atmospheric pressure is playing a significant role. However, much is left to be done. This includes exploring the role of metallicity on the formation of molecular clouds in these systems. It further includes understanding how star formation and its accompanying ultraviolet radiation affects the trends, and providing scaling relations useful in galaxy formation models.

Analytic models of molecular cloud formation are governed significantly by gas density and gas metallicity (Krumholz et al. 2008). Furthermore, Ostriker et al. (2010) suggested that heating of the interstellar gas plays a critical role in controlling both  $H_2$  formation and star formation. In their model, the thermal pressure adjusts to match the midplane pressure set by gravity in disk galaxies. This coupling may then explain the tight correlation between midplane pressure and higher ratios of  $H_2$  to HI surface density in late-type galaxies (Blitz & Rosolowsky 2004, 2006). In our systems the thermal pressure is also governed largely by gravity and so is broadly consistent with this idea.

The constraints provided here may be useful in modeling galaxy formation (e.g., Popping et al. 2014). The role of feedback is crucial and well studied in our systems, and thus may provide insight into how galaxies and their nuclear black holes form and evolve. Radio-mechanical feedback incorporated into semi analytic models and simulations have successfully reproduced several properties including the galaxy luminosity function (Bower et al. 2006b; Croton et al. 2006), the average star formation rate and metallicity over time (Monaco et al. 2007; Robertson & Kravtsov 2008), the mix of cold gas in galaxies and its pressure and metallicity dependence (Krumholz et al. 2008; Obreschkow et al. 2009; Fu et al. 2012; Lagos et al. 2011), and the suppression of cooling atmospheres by AGN (De Lucia & Blaizot 2007). The work presented here takes the work of Blitz & Rosolowski to higher masses and pressures found in early-type galaxies without disks.

Recently, Morselli et al. (2020) analyzed the HI and  $H_2$  content of five nearby, massive main sequence galaxies and linked the availability of molecular and neutral hydrogen to the star formation rate of each region. They found that  $H_2/HI$  increases with gas surface density, and at fixed total gas surface density it decreases (increases) for regions with a higher (lower) specific star formation rate. Morselli et al. (2021) studied the evolution of the  $H_2/HI$  mass ratio with redshift. They found that  $H_2/HI$  within the optical radius slightly decreases with redshift, contrary to common expectations of galaxies becoming progressively more dominated by molecular hydrogen at high redshifts. We are unable to explore this relation due to the low redshift range of our sample.

#### 5. CONCLUSIONS

The relationship between molecular gas mass and hydrostatic pressure for 76 central galaxies in clusters, groups and early-type galaxies is explored. A trend is found between molecular gas mass and hydrostatic pressure measured at an altitude of 10 kpc. The trend follows the power-law slope  $1.9 \pm 0.3$ . This trend with pressure and a similar trend with atmospheric gas density are broadly consistent with the molecular gas having cooled and condensed from the hot atmospheres. We examined the dependence of the  $H_2/HI$  mass ratio with pressure for objects with HI measurements. This ratio exceeds unity in all systems, consistent with ratios found in high pressure regions of spiral galaxies. Our analysis is consistent with a picture where molecular clouds form rapidly from atomic hydrogen in dense, high-pressure atmospheres. Atmospheric pressure may also serve as a “valve” that regulates level of inflow to and outflow from the nuclear black hole (Voit et al. 2020). Thus pressure may be an important factor determining both the production of nuclear fuel and the level of feedback produced by it.

BRM acknowledges support from the Natural Sciences and Engineering Research Council of Canada, and the hospitality of the Flatiron Institute where this paper germinated. This research has made use of data obtained from the Chandra Data Archive and the Chandra Source Catalog, and software provided by the Chandra X-ray Center (CXC) in the application packages CIAO, ChIPS, and Sherpa. We thank all the staff members involved in the Chandra project. Additionally we have used ADS facilities.

#### REFERENCES

- Annis, J., & Jewitt, D. 1993, MNRAS, 264, 593
- Arnaud, K. A. 1996, in Astronomical Society of the Pacific Conference Series, Vol. 101, Astronomical Data Analysis Software and Systems V, ed. G. H. Jacoby & J. Barnes, 17
- Babyk, I. V., McNamara, B. R., Nulsen, P. E. J., et al. 2018, ApJ, 862, 39
- Babyk, I. V., McNamara, B. R., Tamhane, P. D., et al. 2019, ApJ, 887, 149
- Behroozi, P. S., Wechsler, R. H., & Conroy, C. 2013, ApJ, 770, 57
- Blitz, L., & Rosolowsky, E. 2004, ApJ, 612, L29
- . 2006, ApJ, 650, 933
- Bower, R. G., Benson, A. J., Malbon, R., et al. 2006a, MNRAS, 370, 645
- . 2006b, MNRAS, 370, 645
- Bregman, J. N. 2007, ARA&A, 45, 221
- Bregman, J. N., Fabian, A. C., Miller, E. D., & Irwin, J. A. 2006, ApJ, 642, 746
- Chung, A., van Gorkom, J. H., Kenney, J. D. P., Crowl, H., & Vollmer, B. 2009, AJ, 138, 1741
- Combes, F., Young, L. M., & Bureau, M. 2007, MNRAS, 377, 1795
- Crawford, C. S., Allen, S. W., Ebeling, H., Edge, A. C., & Fabian, A. C. 1999, MNRAS, 306, 857
- Croton, D. J., Springel, V., White, S. D. M., et al. 2006, MNRAS, 365, 11

- De Lucia, G., & Blaizot, J. 2007, *MNRAS*, 375, 2
- Dekel, A., Birnboim, Y., Engel, G., et al. 2009, *Nature*, 457, 451
- Donahue, M., de Messières, G. E., O’Connell, R. W., et al. 2011, *ApJ*, 732, 40
- Draine, B. T., & Salpeter, E. E. 1979, *ApJ*, 231, 438
- Edge, A. C. 2001, *MNRAS*, 328, 762
- Edge, A. C., Wilman, R. J., Johnstone, R. M., et al. 2002, *MNRAS*, 337, 49
- Elmegreen, B. G. 1993, *ApJ*, 411, 170
- Fabian, A. C. 1994, *ARA&A*, 32, 277
- . 2012, *ARA&A*, 50, 455
- Feigelson, E. D., & Nelson, P. I. 1985, *ApJ*, 293, 192
- Ford, H. A., & Bregman, J. N. 2013, *ApJ*, 770, 137
- Fu, J., Kauffmann, G., Li, C., & Guo, Q. 2012, *MNRAS*, 424, 2701
- Goudfrooij, P., Hansen, L., Jorgensen, H. E., & Norgaard-Nielsen, H. U. 1994, *A&AS*, 105, 341
- Haynes, M. P., & Roberts, M. S. 1979, *ApJ*, 227, 767
- Hogan, M. T., McNamara, B. R., Pulido, F. A., et al. 2017, *ApJ*, 851, 66
- Isobe, T., Feigelson, E. D., & Nelson, P. I. 1986, *ApJ*, 306, 490
- Kelly, B. C. 2007, *ApJ*, 665, 1489
- Krumholz, M. R., Dekel, A., & McKee, C. F. 2012, *ApJ*, 745, 69
- Krumholz, M. R., McKee, C. F., & Tumlinson, J. 2008, *ApJ*, 689, 865
- Lagos, C. D. P., Baugh, C. M., Lacey, C. G., et al. 2011, *MNRAS*, 418, 1649
- Lakhchaura, K., Werner, N., Sun, M., et al. 2018, *MNRAS*, 481, 4472
- Le Bourlot, J., Le Petit, F., Pinto, C., Roueff, E., & Roy, F. 2012, *A&A*, 541, A76
- Leroy, A. K., Walter, F., Brinks, E., et al. 2008, *AJ*, 136, 2782
- McDonald, M., Veilleux, S., & Mushotzky, R. 2011, *ApJ*, 731, 33
- McDonald, M., Veilleux, S., Rupke, D. S. N., & Mushotzky, R. 2010, *ApJ*, 721, 1262
- McNamara, B. R., Bregman, J. N., & O’Connell, R. W. 1990, *ApJ*, 360, 20
- McNamara, B. R., & Nulsen, P. E. J. 2007, *ARA&A*, 45, 117
- . 2012, *New Journal of Physics*, 14, 055023
- Monaco, P., Fontanot, F., & Taffoni, G. 2007, *MNRAS*, 375, 1189
- Morselli, L., Renzini, A., Enia, A., & Rodighiero, G. 2021, *MNRAS*, 502, L85
- Morselli, L., Rodighiero, G., Enia, A., et al. 2020, *MNRAS*, 496, 4606
- Obreschkow, D., Croton, D., De Lucia, G., Khochfar, S., & Rawlings, S. 2009, *ApJ*, 698, 1467
- O’Dea, C. P., Baum, S. A., Maloney, P. R., Tacconi, L. J., & Sparks, W. B. 1994, *ApJ*, 422, 467
- O’Dea, C. P., Payne, H. E., & Kocevski, D. 1998, *AJ*, 116, 623
- Olivares, V., Salome, P., Combes, F., et al. 2019, *A&A*, 631, A22
- Oosterloo, T., Morganti, R., Crocker, A., et al. 2010, *MNRAS*, 409, 500
- Ostriker, E. C., McKee, C. F., & Leroy, A. K. 2010, *ApJ*, 721, 975
- Popping, G., Somerville, R. S., & Trager, S. C. 2014, *MNRAS*, 442, 2398
- Pulido, F. A., McNamara, B. R., Edge, A. C., et al. 2018, *ApJ*, 853, 177
- Putman, M. E., Peek, J. E. G., & Jounge, M. R. 2012, *ARA&A*, 50, 491
- Robertson, B. E., & Kravtsov, A. V. 2008, *ApJ*, 680, 1083
- Russell, H. R., Sanders, J. S., & Fabian, A. C. 2008, *MNRAS*, 390, 1207
- Russell, H. R., McNamara, B. R., Fabian, A. C., et al. 2019, *MNRAS*, 490, 3025
- Sadler, E. M., & Gerhard, O. E. 1985, *MNRAS*, 214, 177
- Salomé, P., & Combes, F. 2003, *A&A*, 412, 657
- . 2004, *A&A*, 415, L1
- Salomé, P., Combes, F., Revaz, Y., et al. 2011, *A&A*, 531, A85
- Salomé, P., Combes, F., Edge, A. C., et al. 2006, *A&A*, 454, 437
- Schmitt, J. H. M. M. 1985, *ApJ*, 293, 178
- Serra, P., Maccagni, F. M., Kleiner, D., et al. 2019, *arXiv e-prints*, arXiv:1907.08265
- Shapiro, K. L., Falcón-Barroso, J., van de Ven, G., et al. 2010, *MNRAS*, 402, 2140
- Sijacki, D., Springel, V., Di Matteo, T., & Hernquist, L. 2007, *MNRAS*, 380, 877
- van Dokkum, P. G., & Franx, M. 1995, *AJ*, 110, 2027
- Vantyghem, A. N., McNamara, B. R., Russell, H. R., et al. 2018, *ApJ*, 863, 193
- Voit, G. M., Bryan, G. L., Prasad, D., et al. 2020, *ApJ*, 899, 70
- Welch, G. A., Sage, L. J., & Young, L. M. 2010, *ApJ*, 725, 100
- Werner, N., McNamara, B. R., Churazov, E., & Scannapieco, E. 2019, *Space Sci. Rev.*, 215, 5
- Westmeier, T. 2018, *MNRAS*, 474, 289
- Young, L. M., Bureau, M., Davis, T. A., et al. 2011, *MNRAS*, 414, 940